ROYAL SOCIETY OF CHEMISTRY

Journal of
Materials Chemistry A

Strain-induced Suppression of the Miscibility Gap in Nanostructured Mg2Si-Mg2Sn Solid Solutions

SCHOLARONE™
Manuscripts

Strain-induced Suppression of the Miscibility Gap in Nanostructured Mg$_2$Si-Mg$_2$Sn Solid Solutions

Su-In Yi[1+], Vahid Attari[2+], Myunghwan Jeong[1], Jie Jian[3], Sichuang Xue[3], Haiyan Wang[3], Raymundo Arroyave[2,]*, Choongho Yu[1,2,]*

[1]Department of Mechanical Engineering, Texas A&M University,
College Station, TX 77843, USA

[2]Department of Materials Science and Engineering, Texas A&M University,
College Station, TX 77843, USA

[3]School of Materials Engineering, Purdue University,
West Lafayette, IN 47907, USA

*Corresponding authors:
chyu@tamu.edu (C.Y.); rarroyave@tamu.edu (R.A.)

[+]Equally contributed to this work.

1

2

ABSTRACT

Solid solutions of Mg_2Si and Mg_2Sn are promising thermoelectric materials owing to high thermoelectric figure-of-merits and non-toxicity, but they may undergo phase separations under thermal cycles due to the presence of miscibility gaps, implying that thermoelectric properties could be significantly degraded during thermoelectric device operation. Here this study investigates the strain-induced suppression of the miscibility gap in solid solutions of Mg_2Si and Mg_2Sn. Separately prepared Mg_2Si and Mg_2Sn powders were made into $(Mg_2Si)_{0.7}(Mg_2Sn)_{0.3}$ mixtures using a high energy ball-milling method followed by spark plasma sintering. Afterwards, the phase evolution of the mixtures, depending on thermal annealing and mixing conditions, was studied experimentally and theoretically. Transmission electron microscopy and X-ray diffraction results display that, despite the presence of miscibility gap in the pseudo-binary phase diagram, the initial mixture of Mg_2Si and Mg_2Sn evolved towards a solid solution state after annealing for 3 hours at 720 °C. Thermodynamic analysis as well as phase-field microstructure simulations show that strain energy due to coherent spinodal effect suppresses the chemical spinodal entirely and prevents phase separation. This strategy to suppress the miscibility gap induced by lattice strain through non-equilibrium processing can benefit the thermoelectric figure-of-merit by maximizing phonon alloy scattering. Furthermore stable solid solutions by engineering phase diagrams have potential to facilitate the reliable long term operation of thermoelectric generators under continuous thermal loads.

INTRODUCTION

Thermoelectric power generation is unique in generating electricity by utilizing low-grade heat that is typically wasted or dissipated to the environment. There have been remarkable progresses in the performance and diversity of thermoelectric materials over the past decade.[1] Magnesium silicide[2-23] is an emerging thermoelectric material owing to its low density, non-toxicity, and abundant raw materials, and affordable cost in contrast to conventional materials containing lead and tellurium. Recently it was reported that thermoelectric performance of magnesium silicide can be remarkably improved when silicon is partially substituted by tin or/and germanium.

This alloyed structure induces not only phonon scattering that suppresses thermal conductivity,[5, 24-27] but also reduces the energy level differences between valleys in the electronic structures,[6-8] increasing the power factor (PF), $S^2\sigma$, where S and σ are thermopower (or the Seebeck coefficient) and electrical conductivity, respectively. Therefore, the thermoelectric performance, which is typically indicated by the thermoelectric figure-of-merit, $ZT = S^2\sigma T/k$, where T is the absolute temperature and k is the thermal conductivity, can be significantly improved. This enhancement is beyond the well-known rule of mixture explanation for composite materials.[28]

The necessary condition to maximize ZT improvement by the alloying is to ensure the homogeneous distributions of Si and Sn (or/and Ge) in the lattice to a level such that phonons as heat carriers and electrons as charge carriers can sense the mixed elements within the range of their characteristic lengths, mean free paths and wavelengths. Hence, it is important to have a homogeneous solid solution of Mg_2Si and Mg_2Sn (or/and Mg_2Ge) during the material synthesis processes. This ideal situation has often been hard to achieve in $Mg_2(Si,Sn,Ge)$ particularly when individual precursor powders were simply mixed for solid-state reactions. Under these processing conditions, compositional heterogeneities are typically inevitable unless a large amount of time and efforts are devoted to material synthesis.

More importantly, Si and Sn in the Si/Sn sublattice of the Mg_2Si/Sn crystal structure have a positive heat of mixing, which leads to immiscibility within the Sn/Si lattice over the entire temperature range in which the mixture exists in the solid state.[5, 9-11, 29] The tendency towards phase separation as well as differences in the processing history of $Mg_2Si_xSn_{1-x}$ mixtures may be the underlying causes for variations in the reported peak ZT values of $Mg_2Si_xSn_{1-x}$, ranging

mostly from 0.8 to 1.3, but this issue remains poorly studied to date. Furthermore, the miscibility gap suggests that $Mg_2(Si,Sn)$ can undergo phase separation under repeated heat cycles during operation. For stable operation without significant performance degradation, it is important to suppress the miscibility gap in order to avoid phase separation.

Here we focus on elastochemical effects and the subsequent morphology changes when the mixing and annealing conditions of Si-rich and Sn-rich phases are varied. It was found that elastic energy such as elastic strains at interfaces between two phases, local lattice distortions and crystal twinning could affect microstructure evolution.[30-35] To provide lattice strain, high energy ball milling and spark plasma (or current-assisted pressure) sintering (SPS) methods were employed. Unlike conventional synthesis methods, both processes have distinct characteristics of high mechanical pressure and short reaction time, which could result in significant strains between grains in polycrystalline materials.

In order to carry out the systematic study described in this work, Mg_2Si and Mg_2Sn powders were prepared separately, and then they were mixed for different time periods with high energy ball milling followed by thermal annealing. The microstructure evolution was observed experimentally and also computed theoretically. We chose 7:3 ratio of Mg_2Si and Mg_2Sn because this composition is located well within the miscibility gap in the $Mg_2Si_xSn_{1-x}$ system, at the processing temperature, as reported in various works—we here note that there is still considerable uncertainty regarding the location of the miscibility gap in the system. The influence of the phase separation on thermoelectric properties were experimentally measured and compared.

EXPERIMENTAL AND SIMULATION METHODS

Material Synthesis

We prepared Mg_2Si powders (P168 in Table 1) and Mg_2Sn powders (P159 in Table 1) doped with 1.5 at% bismuth for the optimum thermoelectric performance[20] by high energy ball milling (Spex SamplePrep 8000M) with Mg turning (99.9%, Across organics), Si powders (99.999%, -100+325 mesh), Sn powders (99.8%, -325 mesh, Alfa aesar), and Bi powders (99.9%, Strem chemicals) using 3 stainless steel balls (0.5 inch in diameter) in stainless steel container for 10 hours at 1725 rpm (Fig. 1). After the ball milling was done separately for Mg_2Si and Mg_2Sn, X-ray diffraction (XRD) with Bruker-AXS D8 advanced Bragg-Brentano X-ray powder

diffractometer was carried out on the powders, as shown in Fig. 2a. The majority of the powders was found to be Mg_2Si or Mg_2Sn with some impurities of residual Mg, Si, and/or Sn. The powders (0.38 g for Mg_2Si and 0.6 g for Mg_2Sn) were sintered at 750 ^oC (Mg_2Si) or 600 ^oC (Mg_2Sn) for 200 seconds using SPS to make ½-inch diameter pellets whose density is higher than 93.5% of the theoretical density (2.0 g/cm^3 or 3.59 g/cm^3 respectively for Mg_2Si and Mg_2Sn). The Mg_2Si and Mg_2Sn pellets after SPS showed sharp XRD peaks without noticeable impurity peaks. The electronic mobility of these samples at room temperature ranging from 80 to 100 $cm^2V^{-1}s^{-1}$ from the Hall measurements was close to literature values,[20, 36] suggesting defects at grain boundaries are not significant.

The Mg_2Si and Mg_2Sn powders were mixed to have a mixture of $(Mg_2Si)_{0.7}(Mg_2Sn)_{0.3}$. This composition is within the miscibility gaps at our processing temperature no matter which of the Mg_2Sn–Mg_2Si assessed pseudo-binary phase diagrams in literature are considered.[26, 37, 38] Therefore, this composition would give us clearer ideas if the two phases are separated or not due to the miscibility gap. According to the phase diagram, two distinct phases are supposed to appear as the samples are annealed. A mixture of Mg_2Si and Mg_2Sn powders (~2 g) was homogenized using the high energy ball miller for 0.1, 2, and 4 min. Then the mixed powders (0.46 g) were sintered using SPS at ~720 °C for 200 seconds. Finally, samples were annealed at 720 °C for 3 and 7 hours in a sealed graphite die under a vacuum environment ($<10^{-4}$ bar) to observe the evolution of the two phases, Mg_2Si and Mg_2Sn.

Thermoelectric Property Characterization

The synthesized pellet was polished with sand papers in order to make both faces flat and shiny. Thermal conductivity (k) was obtained by measuring thermal diffusivity (D) with Xe-flash apparatus (TA instrument FL3000) since $k = D·\rho·c_p$, where ρ is the density measured using Archimedes method, and c_p is the specific heat[29, 36, 39] from literature. For the measurement of thermopower and electrical conductivity, the pellets were cut into a bar whose dimension is 1.3 × 5 × 11 mm^3 using a diamond saw, and then mounted to our custom-built setup. Electrical conductivity was obtained from the slope of voltage as a function of supplied current ranging from -0.05 A to 0.05 A and the geometry of the samples. Thermopower was obtained from the slope of voltage with respect to temperature difference ranging from -15 K to 15 K. Hall

measurements were carried out using a custom-built setup under 1T magnetic field at room temperature.

Phase Field Approach

The total free energy functional (F^{tot}) for an undeformed material configuration with confined boundaries can be constructed from the sum of all contributing fields over it. F^{tot} can be a functional of composition (c), strain (ε), gradients of composition (∇c), and other fields if present. We write the total free energy functional, F^{tot} as the sum of contributing fields:

$$F^{tot}(c, \varepsilon, \nabla c) = f^{chem} + f^{elas} \tag{1}$$

where chemical free energy density, f^{chem}, and elastic strain energy density, f^{elas} are:

$$f^{chem}(c, \nabla c) = \int_\Omega [\varkappa(\nabla c)^2 + f^{bulk}(c)] \, d\Omega \tag{2}$$

$$f^{elas}(\varepsilon) = \frac{1}{2}\int_\Omega \varepsilon^{el} \sigma^{el} d\Omega \tag{3}$$

where $\varkappa$ is the gradient energy coefficient, and f^{bulk} is the contribution of the bulk phases in the microstructure. ε^{el} and σ^{el} are the local elastic strain and stress in the material. The chemical free energy is composed of the interfacial and bulk energy contributions, and it determines the compositions and volume fractions of the equilibrium phases. The strain energy affects the equilibrium compositions and volume fractions of the coexisting phases, but also determines the shapes and configurations of the phase domains. In an inhomogeneous solid solution, the generalized potential for phase transformation, μ^{tot}, as a function of the concentration, the deviations in concentration, and the elastic strain can be calculated by means of the given free energy functional in Eq. (1) as:

$$\mu^{tot}(c, \varepsilon, \nabla c) = \frac{\delta F^{tot}}{\delta c} = \frac{\partial F^{tot}}{\partial c} - \nabla.\left(\frac{\partial F^{tot}}{\partial \nabla c}\right) \tag{4}$$

$$\mu^{tot} = \frac{\partial f}{\partial c} - \nabla.(\varkappa \nabla c) + \nabla c.\frac{\partial \varkappa}{\partial c}\nabla c - 2\nabla\varepsilon^0(c):\boldsymbol{C}(c)(\varepsilon^{el}) + \left(\varepsilon^{el}:\nabla\boldsymbol{C}(c)(\varepsilon^{el})\right) \tag{5}$$

The separation process of two distinct phases from a homogeneous solution due to small fluctuations in the composition is the case where the system is unstable, and chemical potential is the main responsible driving force for this uphill diffusion process leading to phase separation, while strain energy acts in the reverse way to mitigate the phase separation most of the time.

From linear kinetic theory, the local mass flux in the presence of a gradient in composition, the diffusion flux (in units of mol m^{-2} s^{-1}) is given by:

$$\vec{J} = -\vec{M}\nabla.\mu^{tot} = -\vec{M}\nabla.\left(\frac{\delta F^{tot}}{\delta c}\right) \tag{6}$$

where $\vec{M}$ is the interface mobility assumed to be constant due to isotropic nature of the crystal structures of the two phases. We postulate the following form of the Cahn-Hilliard (C-H) kinetic equation to study the evolution of Mg$_2$Si-Mg$_2$Sn microstructure in 2-dimensioanl (2D), and 3-dimensional (3D) space:

$$\frac{\partial c}{\partial t} = \nabla.\vec{M}\nabla(\mu^{tot}) \tag{7}$$

Given an initial microstructure, the evolution of the microstructure can be studied by solving the Cahn–Hilliard equation using a semi-implicit spectral approach in the Fourier space. The elastic energy contribution to the kinetics of evolution is obtained using the microelasticity theory.[40, 41] There are three factors contributing to the elastic potential: (1) the lattice misfit between the different phases, (2) the elastic constant inhomogeneity, and (3) externally applied stress. In this study, no external force is applied. The microelasticity problem is posed as:

$$\frac{\partial \sigma_{ij}}{\partial r_j} = 0 \text{ in } \Omega \tag{8}$$

$$\varepsilon_{kl} = \frac{1}{2}\left\{\frac{\partial u_k}{\partial r_l} + \frac{\partial u_l}{\partial r_k}\right\} \tag{9}$$

$$\sigma_{ij}^{el} = C_{ijkl}\varepsilon_{kl}^{el} \text{ where } \varepsilon_{kl}^{el} = \varepsilon_{kl}^{tot} - \varepsilon_{kl}^0 \tag{10}$$

Equations (8), (9), (10) are the mechanical equilibrium condition, kinematics, and Hook's microscopic constitutive law for linear elasticity, respectively. ε_{kl}^{el} is the difference between the total strain ε_{kl}^{tot} and the eigenstrain ε_{kl}^0. The dilatational eigenstrain term is $\varepsilon_{kl}^0 = \epsilon^T \delta_{kl} h(c)$, and it is the consequence of lattice strain between the phases. The lattice misfit is $\epsilon^T = (a^\alpha - a^\beta)/0.5(a^\alpha + a^\beta)$ where a^α and a^β are the lattice parameters of α and β phases, respectively. δ_{kl} is the Kronecker-delta function and $h(c)$ is an interpolation function. C_{ijkl} is the composition-dependent fourth order elastic modulus tensor. It is convenient to describe C_{ijkl} using the following expression:

$$C_{ijkl}(c) = C_{ijkl}^{eff} - g(c)\Delta C_{ijkl} \tag{11}$$

where $\Delta C_{ijkl} = C_{ijkl}^\alpha - C_{ijkl}^\beta$ is the difference between the elastic moduli tensor of α and β phases. Similar to $h(c)$, $g(c)$ is a scalar interpolation function such that $h(c_\alpha) = g(c_\alpha) = 0$ and

$h(c_\beta) = g(c_\beta) = 1$. Having a periodic boundary condition, the higher-order solutions for the system of equations (8), (9) and (10) is obtained in the Fourier space based on the lower-order approximations in an iterative manner. A semi-implicit Fourier spectral approach[42] for C-H equation is used.

RESULTS AND DISCUSSION
X-ray diffraction and energy dispersive spectroscopy analysis

P169, P172, P174, P170, and P173 in Table 1 shows a list of samples prepared by mixing Mg_2Si and Mg_2Sn powders with a molar ratio of 7:3. According to a recent paper,[26] this composition is placed at the center of the miscibility gap in the Mg_2Si-Mg_2Sn binary material system so an equal amount of separated phases, $Mg_2Si_{0.5}Sn_{0.5}$ and $Mg_2Si_{0.87}Sn_{0.13}$ are expected to be obtained as they go through mixing and thermal processing at ~720 °C. XRD results in Fig. 2b show phase evolution as the mixture of Mg_2Si and Mg_2Sn went through longer high energy ball milling and thermal annealing.

Surprisingly, as shown in Fig. 2b, the peak pairs (same crystal plane) from Si-rich and Sn-rich $Mg_2Si_xSn_{1-x}$ were merged with longer mixing and annealing, which is opposite to what the phase diagrams in literature describe. We carried out detailed analysis near the major two peak locations (111) in Fig. 2c and (220) in Fig. 2d. Sample P169 with short 0.1-min mixing showed distinct two peaks from Sn-rich and Si-rich phases. In Fig. 2c, we noticed that the (111) peak from the Si-rich phase at 24.23° is close to 24.241° from JCPDS 00-035-0773 for Mg_2Si and has a relatively narrow full width at half maximum (FWHM), but the (220) peak at ~23.1° from the Sn-rich phase is broad, and shifted toward a higher angle compared to 22.747° from JCPDS 00-007-0274 for Mg_2Sn. Another peak at ~24.0° in the middle was also found, suggesting that some of the two phases were miscible. The shifted, broad peak corresponding to Sn-rich phase is likely to indicate that the Sn-rich phase was strained by the Si-rich phase. Considering the lower melting point of Mg_2Sn (778 ℃) compared to Mg_2Si (~1085 ℃) (SPS temperature, 720 ℃), it is probable that softened Mg_2Sn was smeared into spaces between Mg_2Si particles, forming separated Mg_2Si and Mg_2Sn islands as shown in the energy dispersive spectroscopy (EDS) results (Fig. 2e).

When the ball milling time was increased to 2 min (P172) and 4 min (P174), the Si-rich peak at ~24.23° was suppressed and the Sn-rich peak became sharper and further shifted, showing two

prominent peaks at ~23.4° and ~24.0°, which are close to the precipitating phases (~23.47° for $Mg_2Si_{0.5}Sn_{0.5}$ and ~24.04° for $Mg_2Si_{0.87}Sn_{0.13}$) according to the miscibility gap of the phase diagrams reported in the literature. However, when the samples were annealed for 3 hours (P170) and 7 hours (P173), the two peaks were merged toward the theoretically calculated peak position at 23.47° for $Mg_2Si_{0.7}Sn_{0.3}$, suggesting suppression of miscibility gap. Similar trends were observed from the (220) plane (Fig. 2d). According to JCPDS, corresponding angles are 37.587° and 40.121° for Mg_2Sn and Mg_2Si, respectively. Two broad peaks close to the two precipitating phases (38.81° for $Mg_2Si_{0.5}Sn_{0.5}$ and 39.77° for $Mg_2Si_{0.87}Sn_{0.13}$) were found from P172 and P174, and then, after thermal annealing, they were merged into a single peak, which is close to 29.32° for $Mg_2Si_{0.7}Sn_{0.3}$. Note that the peak angle locations for the solid solutions ($Mg_2Si_{0.5}Sn_{0.5}$, $Mg_2Si_{0.7}Sn_{0.3}$, $Mg_2Si_{0.87}Sn_{0.13}$) were calculated from the lattice constants obtained by interpolation with the lattice constants of Mg_2Si and Mg_2Sn.

The EDS results (Fig. 2e) from Sample P169 showed segregated Sn-rich and Si-rich phases, whose dimensions are less than 100 nm. On the other hand, the EDS results in Fig. 2e for Sample P170 with 3-hour annealing displayed dull colors with smaller reddish and greenish regions, suggesting a much better degree of mixing although relatively richer Si and Sn regions are observable. Nevertheless the XRD results for P170 showed only merged peaks. Despite the presence of varying compositions according to the EDS results, the XRD results show merged peaks corresponding to a homogeneous solid solution. In fact, similar results are also displayed in other papers.[9, 29] Therefore we can conjecture that the small grains are strained. To maintain the strain, coherent boundaries may be present like other samples prepared similarly using ball milling and SPS processes.[36]

Phase stability analysis in Mg_2Si-Mg_2Sn pseudo-binary system

Our XRD and EDS results indicate that Mg_2Si and Mg_2Sn are miscible in the composition and the processing temperature (X_{Si}=0.7 at 720 °C) in this study. A close look at the available pseudo-binary phase diagram of Mg_2Sn-Mg_2Si system suggests that there are considerable uncertainties in the location of the Sn-rich and Si-rich phase boundaries in the Mg_2Sn-Mg_2Si pseudo-binary system, as shown in Fig. 3a. Except for the study by Nikitin *et al.*,[43] other experimental and theoretical assessments[26, 37, 38, 44, 45] show that the selected composition, and

temperature is located well within the chemical miscibility region of the phase diagram, as discussed below.

Considering the location of the Sn-rich phase boundary in the Mg_2Sn-Mg_2Si pseudo-binary, all experimental evidence presented to date suggests that this boundary is located within the $0.1<X_{Si}<0.45$ range near our processing temperature. Over a wide temperature range, Muntyanu et al.,[44] Nikitin et al.,[43] and Jung et al.[45] show that this boundary is within the $0.35<X_{Si}<0.45$ range. Kozlov et al.[37] carried out experimental investigations on this system and performed an assessment of its phase stability based on their own data as well as any other existing phase stability information published prior to their work. Their assessed pseudo-binary phase diagram indicates that the phase boundary is around $X_{Si}\sim0.1$ at our processing temperature. In a later assessment by Viennois et al.,[38] this phase boundary is located at $X_{Si}\sim0.3$, somewhat in between the analysis by Kozlov and Nikitin/Jung. The most recent investigation on the phase stability on this system was carried out by Vives et al.,[26] who performed diffusion couple experiments over a wide range of temperatures and identified $X_{Si}\sim0.4$ as the location of the Sn-rich phase boundary in the Mg_2Sn-Mg_2Si miscibility gap. While there is evidently considerable uncertainty as to the exact location of this phase boundary, the composition used in this study, $X_{Si}=0.7$, is clearly to the right of all assessed solubility limits for Si in Mg_2Sn.

When looking at the Si-rich phase boundary, we would like to note that every single investigation of the system, except for Nikitin et al. indicates that the alloy investigated in this work is to the left of the Si-rich phase boundary (Sn solubility limit for Mg_2Si). This phase boundary is located around $X_{Si}\sim0.9$ in the study by Muntanyu et al., Jung et al., Viennois et al., and Vives et al., Kozlov et al. locate this boundary at slightly lower values of Si, $X_{Si}\sim0.78$. Out of all the existing evidences, only the assessed Si-rich phase boundary by Nikitin et al. places our alloy outside the miscibility gap (to the right of the Si-rich phase boundary).

A thorough analysis of this apparent inconsistency was carried out by Kozlov et al., who compared their own differential scanning calorimetry and thermal analysis analysis for different alloys as well as the phase constitution and composition of solidified alloys belonging to this system and conclusively showed that the phase boundary reported by Nikitin et al. could not be reconciled with available data. Perhaps an even stronger piece of evidence that puts into question the results by Nikitin et al. is the diffusion couple study by Vives et al. which suggest that the phase boundary is closer to $X_{Si}\sim0.9$, in agreement with five decades worth of research on this

system and in contradiction with Nikitin *et al.* Given the preponderance of evidence, we are confident that the alloy investigated in this work is well-within the Mg$_2$Sn-Mg$_2$Si bulk chemical miscibility gap.

In the present study, however, under the non-equilibrium synthesis conditions, it is not clear that the system phase separates in the composition (X_{Si}=0.7) well within the miscibility gap. Here we investigate the possible underlying reasons for this observation from a thermodynamic perspective using Eq. 1. We use the pseudo-binary phase diagram obtained by Viennois *et al.*[38] Assuming ideal entropy of mixing, Viennois *et al.* proposed the following equation for calculating the mixing Gibbs energy, $\Delta_{mix}G$:

$$\Delta_{mix}G(\mathrm{Mg2}/_3 X c/_3 Y_{(1-c)}/_3) = \Delta_{mix}H(\mathrm{Mg2}/_3 X c/_3 Y_{(1-c)}/_3) + \frac{RT}{3}(c_i \ln c_i + (1-c_i)\ln(1-c_i)) \quad (12)$$

where the mixing enthalpy, $\Delta_{mix}H$ shown in Fig. 3b, was obtained using a fit of $\Delta_{mix}E$ with Redlich-Kister polynomials as in standard CALPHAD approaches and X=Si and Y=Sn in this formulation. Hence, the mixing Gibbs energy can be rewritten as:

$$\Delta_{mix}G(\mathrm{Mg2}/_3 X c/_3 Y_{(1-c)}/_3) = \sum_{i=1}^{n-1}\sum_{j=i+1}^{n} c_i c_j L_{ij} + \frac{RT}{3}(c_i \ln c_i + (1-c_i)\ln(1-c_i)) \quad (13)$$

with $L_{ij} = \sum_{v=0}^{k}(c_i - c_j)^v \, {}^v L_{ij}$, where ${}^v L_{ij}$ is the temperature invariant interaction parameter. $c_i = c_{Sn}$ and $c_j = c_{Si}$. ${}^0 L_{ij}$ and ${}^1 L_{ij}$ are 5950 and -800 J/mol, respectively and the two parameters are sufficient for the parameterization of the subregular-solution model.[46] The mixing Gibbs energies at 420, 520, 620, 720 and 820 °C are shown in Figure 3c. A close look at the pseudo-binary free energy curves reveals that the double-well free energy and hence the miscibility gap diminishes by increasing the temperature due to the entropic stabilization, and closes at ~845 °C.

In addition to chemical contributions, we consider the local contractions/expansions upon phase transformation, which produce additional strain energy terms. By replacing F^{chem} with $\Delta_{mix}G$ in Eq. 10 and, following the approach proposed by Cahn,[30] we write the following total free energy for the material:

$$F^{tot} = \Delta_{mix}G(\mathrm{Mg2}/_3 X c/_3 Y_{(1-c)}/_3) + \int_{\Omega_m} \frac{2\alpha_c^2 E}{1-v}(c - c_0)^2 \, d\Omega_m \quad (14)$$

where the second term is the total elastic energy of an isotropic solid with arbitrary composition fluctuations. In the last term, Ω_m is the molar volume, α_c is the Vegrad's parameter ($\alpha_c = \varepsilon_{ii}^{\sigma=0}/\delta c$), where $\varepsilon_{ii}^{\sigma=0}$ is the stress-free dilatational strain. E is the Young Modulus, v is the Poisson's ratio, and c_0 denotes the overall (average) composition of the material. Fig. 3c compares the calculated elastochemical free energies with the chemical curves at different temperatures. Eventually, these calculations depict the gradual conversion of double-wells into parabolas at temperatures around ~680 to ~845 °C due to elastic interactions. These results infer that the coherency strains stabilize the material against infinitesimal composition changes at this temperature range which is in agreement with our experimental observations.

The boundaries of the elastochemical pseudo-binary miscibility gap and spinodal lines for the Mg_2Sn-Mg_2Si were calculated by linear stability analysis, as shown in Fig. 3a. In calculation of these lines we have assumed the validity of small-strain elasticity theory in an isotropic system neglecting any other change in excess thermodynamic quantities. The parameters used to obtain these curves are summarized in Table 2. The figure illustrates the experimental point in the present work and the pseudo-binary phase diagram by Kozlov *et al.* The point that is indicated by the inverse triangle resides in the chemical spinodal region. However, it is above the obtained elastochemical miscibility gap indicating the tendency to form a solid solution under highly non-equilibrium processing conditions.

The important concept of intrinsic stability and thermodynamics of systems under externally controlled thermodynamic variables are originally coined by Gibbs,[47] Tisza,[48] Cahn,[49] Huh-Johnson.[50] It is well established that to have an intrinsic instability it is necessary to have at least one negative eigenvalue for the hessian matrix of the second derivative of free energy functional with respect to infinitesimally small perturbations. Following the limit of metastability, we have spanned the chemical miscibility line around the strain, composition and temperature space. Figure 3d shows the obtained three-dimensional phase diagram in strain-composition-temperature space. The pseudo-binary phase diagram by Kozlov *et al.* resides at $\varepsilon = 0$, which corresponds to the bulk state. In this figure, two subsets of lines are present for constant strains and constant temperatures indicated by vertical and horizontal brown lines, respectively. The elastochemical miscibility line in Fig. 3a is a subset of this space along constant strain.

Phase field modeling of Mg$_2$Sn-Mg$_2$Si microstructural evolution

In order to further analyze this unusual observation of suppression of a solid miscibility gap, the evolution of the microstructure was investigated through phase field kinetics simulation based on the structural configuration from EDS analysis for mapping the distribution of Sn and Si atoms (Fig. 2e) (sample P169). Individual distribution information of Sn and Si atoms from EDS was post-processed so as to obtain the microscopic stoichiometry of x in Mg$_2$Si$_x$Sn$_{1-x}$ with the resolution of 1~2 nm. The initial microstructure for 2D simulation was obtained from the EDS data of P169. The initial condition in the 3D case is a generated synthetic microstructure based on the average grain value of Mg$_2$Sn phases from EDS data of P169.

Then, both 2D and 3D synthetic microstructures were computationally annealed for 3 hours at 720 °C. We comparatively investigated the strain effect in addition to the chemical effect. The distribution of the elastic strains ($\varepsilon_{xx}^{elas}, \varepsilon_{yy}^{elas}, \varepsilon_{xy}^{elas}$), and the values along the line (*) are shown in Fig 4. The calculations show that Mg$_2$Sn phases are under compressive strains. Figure 5 compares the evolution of the microstructure for chemical only and elastochemical regimes. When only chemical interactions were considered, the microstructure followed the normal spinodal decomposition route, and the microstructure became more locally segregated and coarser over time. In this case, the gradient energy coefficient ($\varkappa$) controls the rate of coarsening. When we considered the strain effects in the model, Mg$_2$Sn phases started to slowly release Sn to the Mg$_2$Si matrix. Eventually, the domain gets dispersed throughout with Sn and Si elements. In the end, the overall molar concentration of Si in the domain reaches to 0.7 over the entire domain. The obtained semi-uniform composition of 0.7 is close to the minimum of the elastochemical free energy curve at 720 ℃ as it is depicted in Fig. 3c. Experimental EDS results in Fig. 2e (sample P170) also suggest that Si and Sn get more dispersed in the domain, and the XRD results also indicate that the two separated peaks were merged after the annealing process. We believe that the system tends to dissolve and form a solid solution, instead of following the phase separation path suggested by the metastable phase diagrams published in the literature.

By matching the simulated microstructures after the isothermal annealing treatment to the experimentally observed microstructure, the free parameters of the model (i.e., mobility and gradient energy coefficient) were estimated. In the case of coherent microstructural evolution, the interfacial mobility and the gradient energy coefficient are estimated to be around 10^{-12} m^2/s and 10^{-1} J/m^2, respectively at 720 °C. Figure 6 illustrates that Si concentration is reduced in

Mg$_2$Si-rich sites and is increased in Mg$_2$Sn-rich sites over time until it reaches an equilibrium value, which corresponds to a degree of immiscibility that is considerably smaller than what is observed in the bulks without such nanoscale crystalline grains. This figure is obtained by tracking the maximum and minimum values of concentration in the simulation cell. In fact, according to our simulations, the composition gap between Si-rich and Sn-rich regions of the microstructure should be no more than about 0.1 in molar concentration units. These results are consistent with the experimental observations showing that the system tends to become more homogeneous after annealing, even in samples that appear to be within the miscibility gap found in bulk phase stability studies.

The influence of phase evolution on thermoelectric transport properties

The thermal conductivity of P169, P172, P174, P170, and P173 whose x is 0.7 in (Mg$_2$Si)$_x$ (Mg$_2$Sn)$_{1-x}$ were measured, as shown in Fig. 7a. The decreasing thermal conductivity as a function of temperature suggests negligible bipolar thermal conductivity, which implies degenerate doping as well as larger band gaps compared to that of Mg$_2$Si$_x$Sn$_{1-x}$ with x = 0.3 as reported in the literature.[6] It is notable that P169 with least mixing of the two phases displayed higher thermal conductivities than those of other samples. It is noteworthy that the thermal conductivities of P172 and P174, whose XRD peaks indicate some degrees of phase separation, are similar to those of P170 and P173 whose XRD peaks from Sn-rich and Si-rich phases were merged. This is good indication that alloy scattering is very effective in dropping thermal conductivity of this system, similarly to other alloys such Si$_x$Ge$_{1-x}$.

Lattice thermal conductivity for two representative samples (P169 – least mixed; P173 – most mixed) were obtained after subtracting the electronic thermal conductivity portion using the Wiedemann Franz law, as shown in Fig. 7b. The higher phase homogeneity in P173 resulted in lower thermal conductivity. The experimental data points were fitted using the modified Callaway model for phase segregated materials.[5] This model considers three simplified components, phase-pure portions (Mg$_2$Si, Mg$_2$Sn) and mixed portions (Mg$_2$Si$_{0.7}$Sn$_{0.3}$). According to the fitting results, P169 with the most distinct two phases has 27% unmixed portion out of the entire volume. It should be noted that Mg$_2$Si$_{0.7}$Sn$_{0.3}$ represents the mixed portions with various compositions (i.e., Mg$_2$Si$_x$Sn$_{1-x}$ where 0<x<1) because even slight alloying drops the thermal conductivity to the values observed from well-mixed samples. Therefore, we could say ~27%

volume of P169 is composed of relatively phase-pure materials and ~73% volume is solid solutions, $Mg_2Si_xSn_{1-x}$ with various compositions. On the other hand, a much smaller (~7%) volume of P173 was estimated to be phase-pure.

Figure 7c and 7d show the electrical conductivity and thermopower measurement data of the representative two samples. The carrier concentrations were measured to be 2.2×10^{20} cm^{-3} for P169 and 2.8×10^{20} cm^{-3} for P173. This suggests that most of the Bi dopant in P169 is active ($Mg_2Si_{0.985}Bi_{0.015}$ and $Mg_2Sn_{0.985}Bi_{0.015}$). The electrical conductivity decreases with temperature, indicating the degenerate doping. The negative sign of thermopower whose magnitude is smaller than 200 μV/K also supports the fact that our samples are heavily-doped n-type semiconductors. The electrical conductivity and thermopower of P173 are similar to those of P169 despite 30% higher carrier concentration compared to P169, which may be attributed to the more significant scattering due to alloy or/and strained grain boundaries in P173.

CONCLUSIONS

Mg_2Si and Mg_2Sn powders were separately prepared, and they were mixed for different time periods using a high energy ball miller. The mixed powders were sintered by SPS and then the sintered pellets were annealed for different time periods to evaluate the evolution of the two phases. We studied 7:3 composition for (Mg_2Si):(Mg_2Sn), which is well within the miscibility gaps reported in literature. According to XRD and EDS results, the two separate phases indicating Mg_2Si-rich regions and Mg_2Sn-rich regions were clearly present when the two powders were gently mixed. With more rigorous mixing, XRD results indicated the two phases are miscible. Upon thermal annealing, XRD peaks from Mg_2Si-rich and Mg_2Sn-rich phases were merged, and EDS results also displayed a much higher degree of mixing, which is inconsistent with the phase diagrams in literature. Our simulation results suggest that strain effects play critical roles in suppressing the miscibility gap for our nanocrystalline structures whereas phase separation could occur when only chemical miscibility gap is present. When the two phases are mixed more or less, lattice thermal conductivity were reduced and electrical transport properties were relatively insensitive to the degree of mixing. Therefore, to maintain high thermoelectric performance, it is recommended to have strain in lattice in order not to fall into the chemical miscibility gap. The strategy to suppress the miscibility gap bears potential impact inasmuch as many thermoelectric materials employ alloyed systems because maintaining alloying structures

for low thermal conductivity could provide the stability and reliability for the actual usage of thermoelectric generator over a long period of time.

ACKNOLWEDGMENT

Table 1. List of samples, $(Mg_2Si)_x(Mg_2Sn)_{1-x}$ experimentally tested for this study along with their synthesis conditions and electrical properties at room temperature.

Sample #	x	Ball milling time (min)	Post annealing time (hour)	Density (%)	Electrical conductivity (S/cm)	Carrier concentration (10^{20} cm^{-3})	Mobility (cm^2/V-s)
P168	1.0	N/A	0	99.5	1270	1.9	41
P169		0.1	0	102	1790	2.2	50
P172		2	0	102	1510	2.3	41
P174	0.7	4	0	102	1420	2.1	42
P170		2	3	96	1620	1.9	53
P173		4	7	97	1870	2.8	42
P159	0.0	N/A	0	93.5	3730	2.3	100

Table 2. Material properties of Mg_2Si and Mg_2Sn.

Phase	Lattice constant (nm)[51]	Elastic constants (GPa)[52, 53]			Young Modulus (GPa)[52, 53]	Poisson coef.	Molar volume (m^3/mol)[54]	Interface mobility (m^2/s) [This work]
		C_{11}	C_{12}	C_{44}				
Mg_2Sn	$6.327 + 6.5 \times 10^{-5}T + 4 \times 10^{-8}T^2$	83.71	39.79	21.69	57	0.2058	1.55×10^{-5}	$\sim 10^{-12}$
Mg_2Si	$6.732 + 8.5 \times 10^{-5}T + 3.8 \times 10^{-8}T^2$	114.07	19.56	33.32	118	0.1464	3.95×10^{-5}	

Figure captions

Figure 1. Material preparation procedures and subsequent thermal annealing and measurements.

Figure 2. XRD results of (a) synthesized Mg_2Si and Mg_2Sn powders and pellets after SPS; (b) mixtures of Mg_2Si and Mg_2Sn in Table 1. Detailed analyses of the XRD results near (c) (111) and (220) planes. Five vertical lines correspond to the peak locations for various Si:Sn ratios: Mg_2Sn, $Mg_2Si_{0.5}Sn_{0.5}$, $Mg_2Si_{0.7}Sn_{0.3}$, $Mg_2Si_{0.87}Sn_{0.13}$, and Mg_2Si. (e) EDS results of P169 and P170.

Figure 3. Calculated (a) Calculated elastochemical miscibility gap versus the chemical gap showing the shift of miscibility gap and spinodal lines due to strain energy impact. Experimental data are taken from literature. The parameters used in calculation of the elastochemical miscibility gap are summarized in Table 2. (b) Enthalpy of formation. (c) Total elastochemical energy curves versus chemical energies at 420 °C, 520 °C, 620 °C, 720 °C, and 820 °C. (d) The three-dimensional strain-composition-temperature phase diagram for Mg_2Si-Mg_2Sn pseudo-binary system. The red and green lines are elastochemical miscibility lines whereas the blue lines are chemical miscibility lines. For comparison, the miscibility gap from Kozlov *et al.* is plotted.

Figure 4. Distribution of elastic strains ($\varepsilon_{xx}^{elas}, \varepsilon_{yy}^{elas}, \varepsilon_{xy}^{elas}$) in the microstructure at the beginning of the simulation, and across the line (*)

Figure 5. Evolution of Mg_2Si-rich and Mg_2Sn-rich phases when elastochemical (top row) or chemical only (bottom row) simulations were considered. (a) Initial condition (Sample 169). 2D and 3D simulation results during the 720 °C annealing process by considering elastochemical interactions after (b) 2 minutes, (c) 30 minutes, (d) 1 hour, and (e) 3 hours, and (f,g,h,i) those by considering only chemical interactions.

Figure 6. Elemental dissolution from Sn and Si lattice sites of Mg_2Sn and Mg_2Si phases toward formation of a solid solution. Estimated dissolutions with a rate of 10^{-12} m^2/s (solid curves) and 10^{-11} m^2/s (dashed curves).

Figure 7. (a) Thermal conductivity of samples, (b) lattice thermal conductivity with calculation results, (c) electrical conductivity, and (d) thermopower.
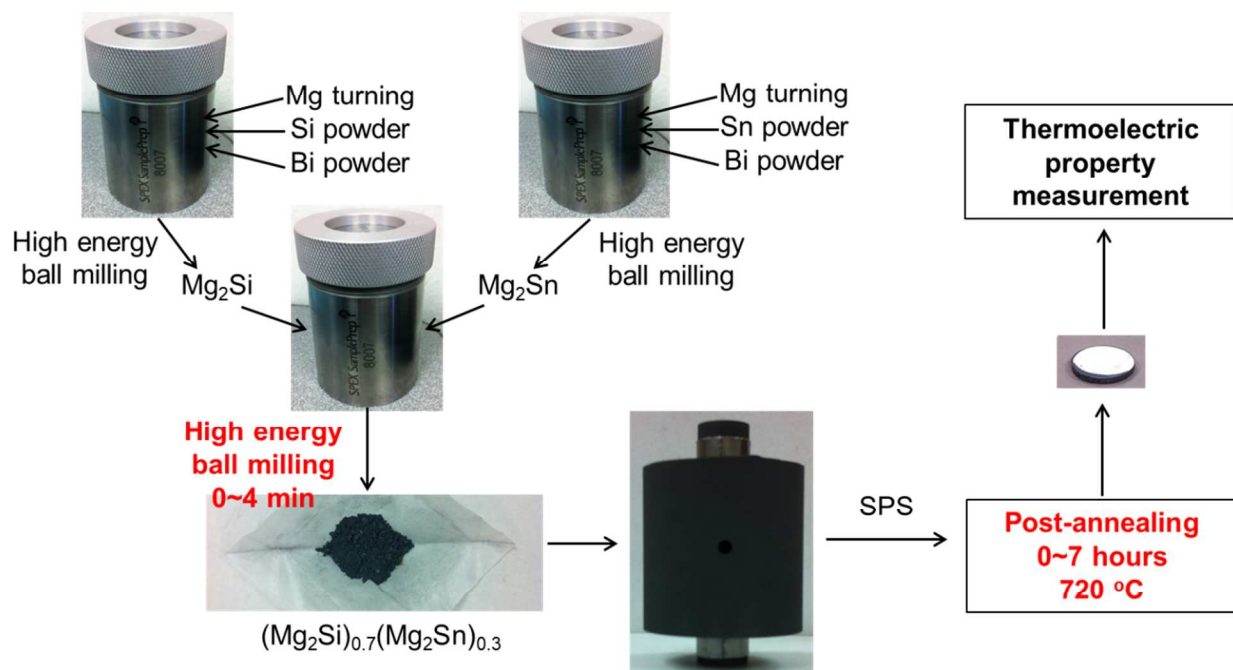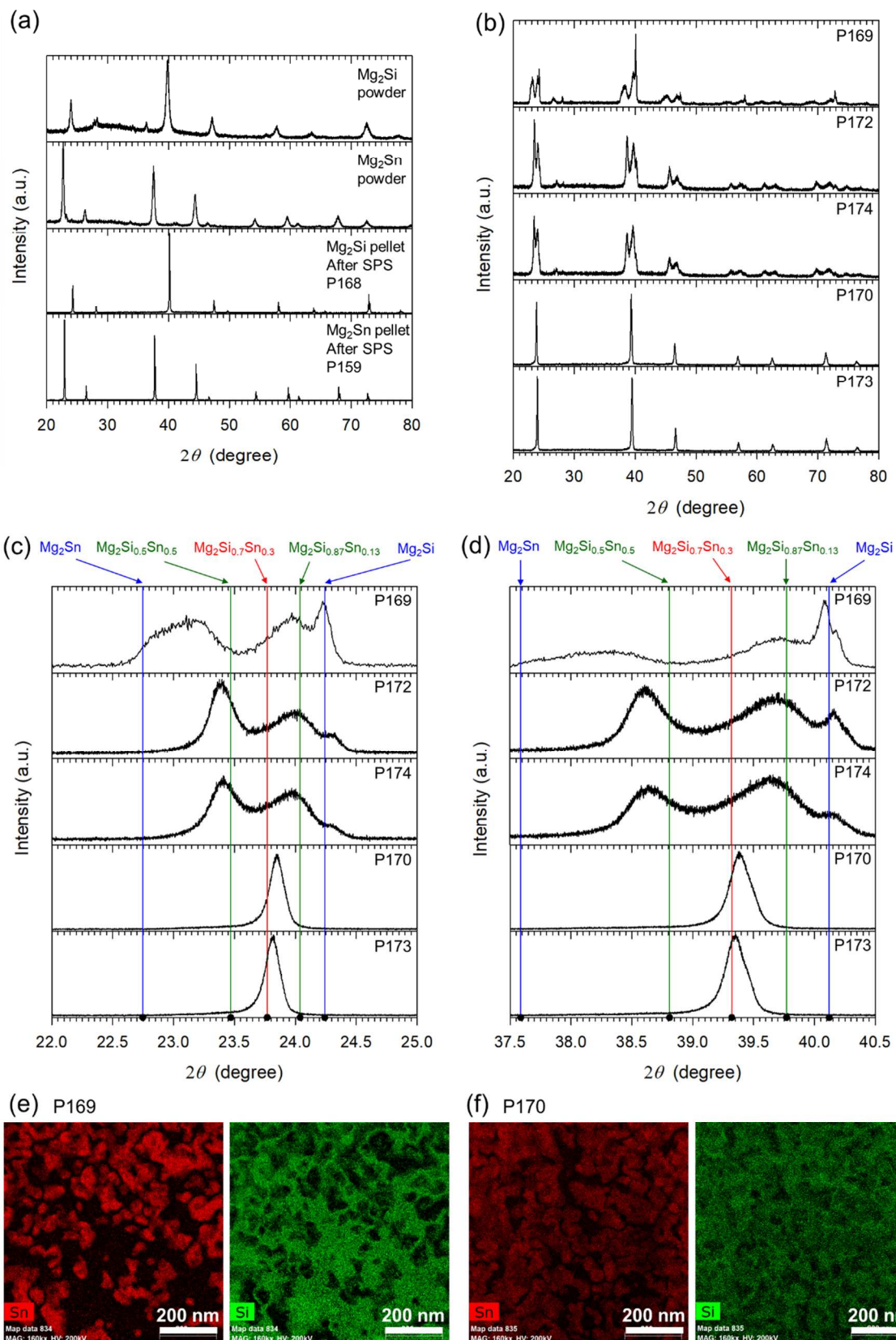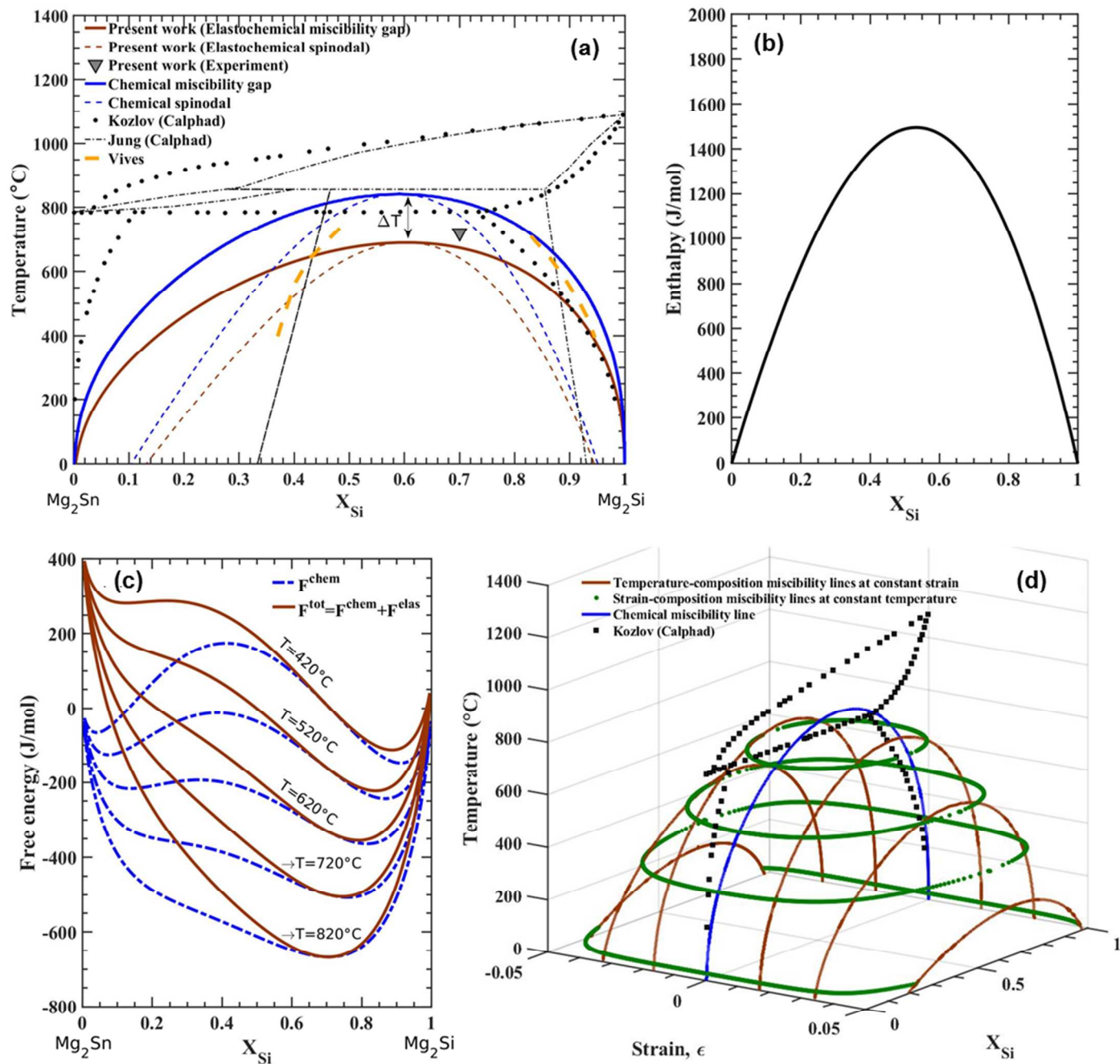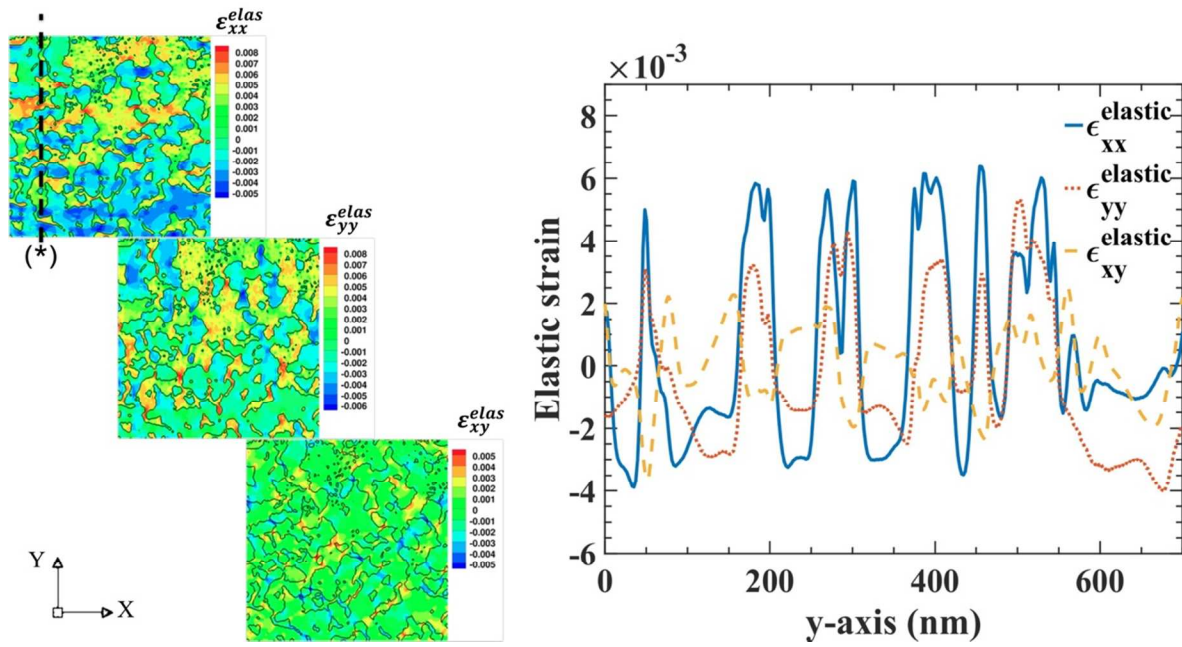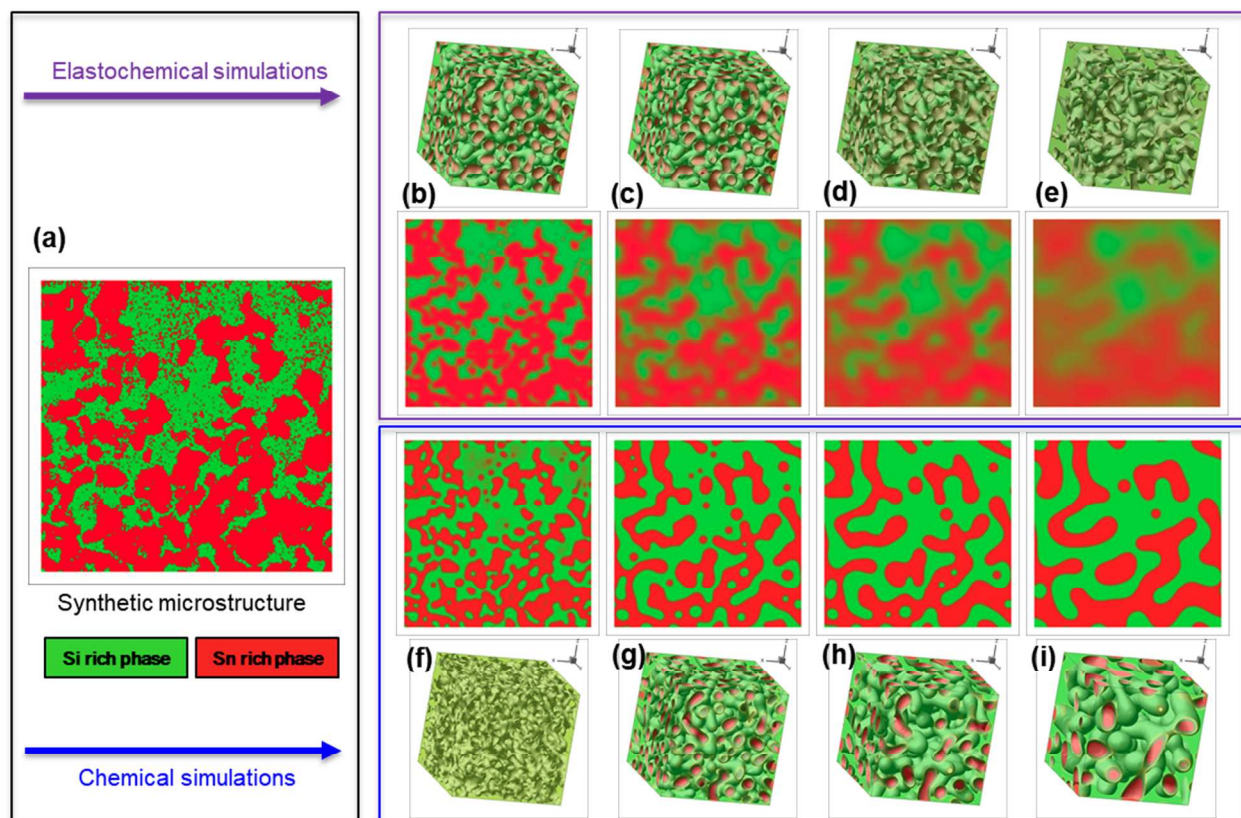
Figure 1.

Figure 2.

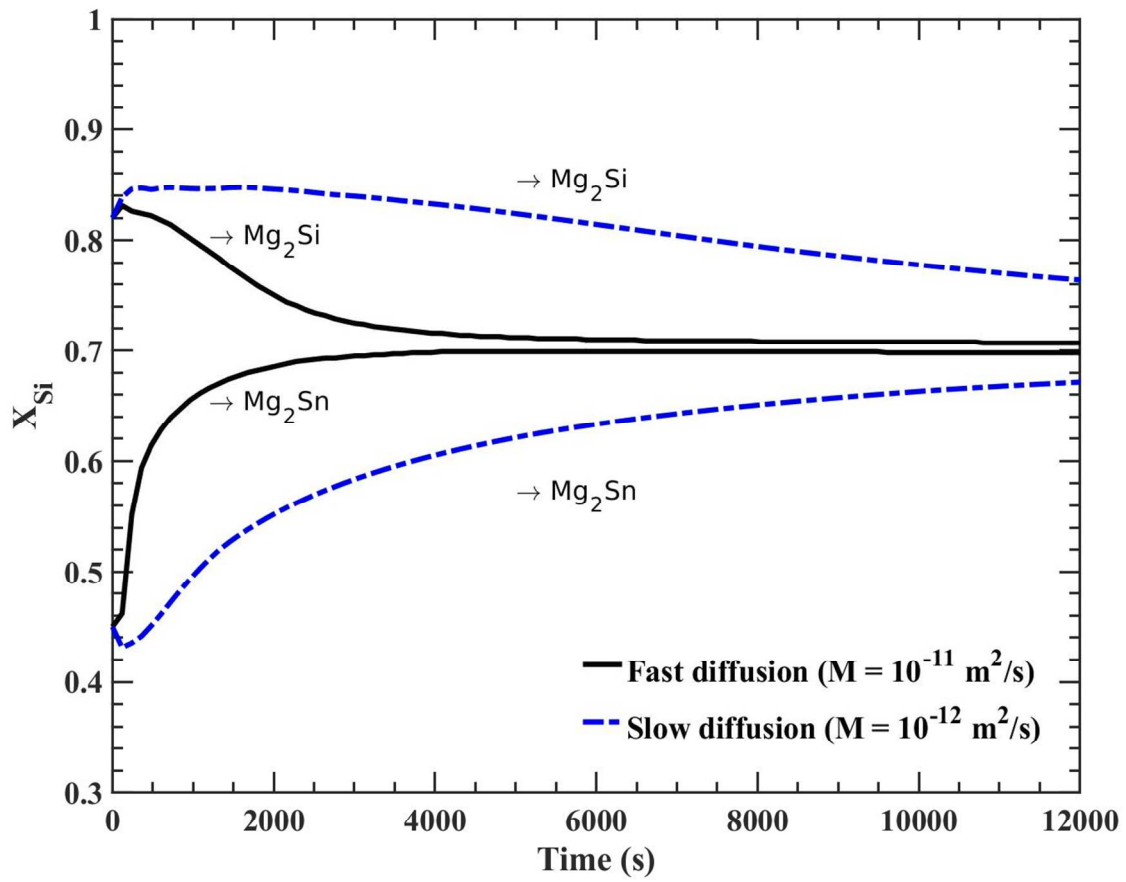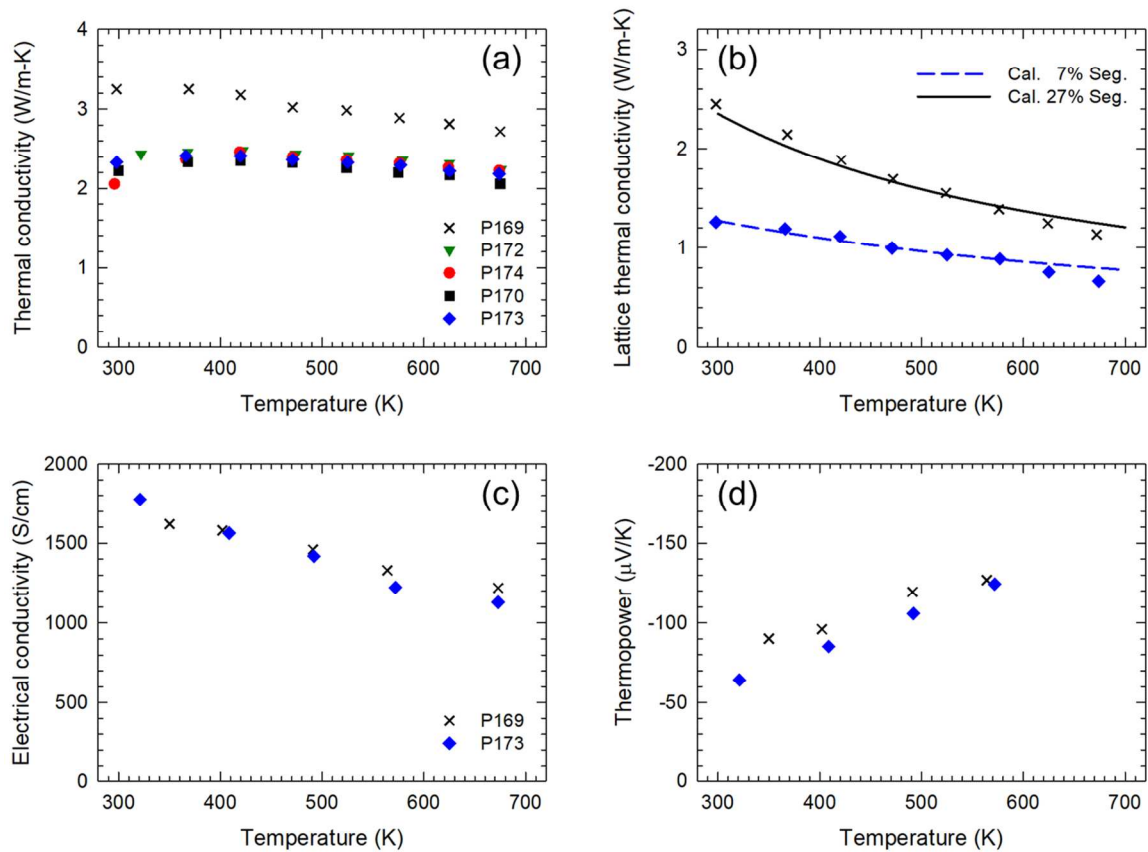**Figure 3.**

**Figure. 4**

Figure 5.

Figure 6.

Figure 7.

REFERENCES

1. L.-D. Zhao, S.-H. Lo, Y. Zhang, H. Sun, G. Tan, C. Uher, C. Wolverton, V. P. Dravid and M. G. Kanatzidis, *Nature*, 2014, **508**, 373.

2. S. I. Kim, K. H. Lee, H. A. Mun, H. S. Kim, S. W. Hwang, J. W. Roh, D. J. Yang, W. H. Shin, X. S. Li and Y. H. Lee, *Science*, 2015, **348**, 109-114.

3. Y. Tang, Z. M. Gibbs, L. A. Agapito, G. Li, H.-S. Kim, M. buongiorno Nardelli, S. Curtarolo and G. J. Snyder, *Nature materials*, 2015, **14**, 1223.

4. J. P. Heremans, V. Jovovic, E. S. Toberer, A. Saramat, K. Kurosaki, A. Charoenphakdee, S. Yamanaka and G. J. Snyder, *Science*, 2008, **321**, 554-557.

5. A. S. Tazebay, S.-I. Yi, J. K. Lee, H. Kim, J.-H. Bahk, S. L. Kim, S.-D. Park, H. S. Lee, A. Shakouri and C. Yu, *ACS applied materials & interfaces*, 2016, **8**, 7003-7012.

6. W. Liu, X. Tan, K. Yin, H. Liu, X. Tang, J. Shi, Q. Zhang and C. Uher, *Physical review letters*, 2012, **108**, 166601.

7. K. Yin, X. Su, Y. Yan, Y. You, Q. Zhang, C. Uher, M. G. Kanatzidis and X. Tang, *Chemistry of Materials*, 2016, **28**, 5538-5548.

8. W. Liu, J. Zhou, Q. Jie, Y. Li, H. S. Kim, J. Bao, G. Chen and Z. Ren, *Energy & Environmental Science*, 2016, **9**, 530-539.

9. G. Polymeris, N. Vlachos, A. Khan, E. Hatzikraniotis, C. B. Lioutas, A. Delimitis, E. Pavlidou, K. Paraskevopoulos and T. Kyratsi, *Acta Materialia*, 2015, **83**, 285-293.

10. Q. Zhang, J. He, X. Zhao, S. Zhang, T. Zhu, H. Yin and T. Tritt, *Journal of Physics D: Applied Physics*, 2008, **41**, 185103.

11. Q. Zhang, J. He, T. Zhu, S. Zhang, X. Zhao and T. Tritt, *Applied Physics Letters*, 2008, **93**, 102109.

12. W. Liu, H. Chi, H. Sun, Q. Zhang, K. Yin, X. Tang, Q. Zhang and C. Uher, *Physical Chemistry Chemical Physics*, 2014, **16**, 6893-6897.

13. P. Gao, X. Lu, I. Berkun, R. D. Schmidt, E. D. Case and T. P. Hogan, *Applied Physics Letters*, 2014, **105**, 202104.

14. X. Liu, T. Zhu, H. Wang, L. Hu, H. Xie, G. Jiang, G. J. Snyder and X. Zhao, *Advanced Energy Materials*, 2013, **3**, 1238-1244.

15. Z. Du, T. Zhu, Y. Chen, J. He, H. Gao, G. Jiang, T. M. Tritt and X. Zhao, *Journal of Materials Chemistry*, 2012, **22**, 6838-6844.

16. J.-i. Tani and H. Kido, *Intermetallics*, 2008, **16**, 418-423.

17. J.-i. Tani and H. Kido, *Computational Materials Science*, 2008, **42**, 531-536.

18. J.-i. Tani and H. Kido, *Intermetallics*, 2007, **15**, 1202-1207.

19. J.-i. Tani and H. Kido, *Physica B: Condensed Matter*, 2005, **364**, 218-224.

20. S. K. Bux, M. T. Yeung, E. S. Toberer, G. J. Snyder, R. B. Kaner and J.-P. Fleurial, *Journal of Materials Chemistry*, 2011, **21**, 12259-12266.

21. M. Akasaka, T. Iida, A. Matsumoto, K. Yamanaka, Y. Takanashi, T. Imai and N. Hamada, *Journal of Applied Physics*, 2008, **104**, 013703.

22. M. Akasaka, T. Iida, T. Nemoto, J. Soga, J. Sato, K. Makino, M. Fukano and Y. Takanashi, *Journal of Crystal Growth*, 2007, **304**, 196-201.

23. G. Nolas, D. Wang and M. Beekman, *Physical Review B*, 2007, **76**, 235204.

24. E. K. Lee, L. Yin, Y. Lee, J. W. Lee, S. J. Lee, J. Lee, S. N. Cha, D. Whang, G. S. Hwang and K. Hippalgaonkar, *Nano letters*, 2012, **12**, 2918-2923.

25. S.-i. Yi and C. Yu, *Journal of Applied Physics*, 2015, **117**, 035105.

26. S. Vivès, P. Bellanger, S. Gorsse, C. Wei, Q. Zhang and J.-C. Zhao, *Chem. Mater.*, 2014, **26**, 4334-4337.

27. L. Yin, E. K. Lee, J. W. Lee, D. Whang, B. L. Choi and C. Yu, *Applied Physics Letters*, 2012, **101**, 043114.

28. D. G. R. William D. Callister, *Materials science and engineering: an introduction*, Wiley, 9th edn., 2013.

29. W. Liu, X. Tang, H. Li, K. Yin, J. Sharp, X. Zhou and C. Uher, *Journal of Materials Chemistry*, 2012, **22**, 13653-13661.

30. J. W. Cahn, *Acta metallurgica*, 1961, **9**, 795-801.

31. J. W. Cahn, *Acta metallurgica*, 1962, **10**, 179-183.

32. F. Larché and J. W. Cahn, *Acta metallurgica*, 1985, **33**, 331-357.

33. R. W. Balluffi, S. Allen and W. C. Carter, *Kinetics of materials*, John Wiley & Sons, 2005.

34. P. Voorhees and W. C. Johnson, *Solid State Physics-Advances in Research and Applications*, 2004, **59**, 1-201.

35. A. G. Khachaturyan, *Theory of structural transformations in solids*, Courier Corporation, 2013.

36. W. Liu, H. S. Kim, S. Chen, Q. Jie, B. Lv, M. Yao, Z. Ren, C. P. Opeil, S. Wilson and C.-W. Chu, *Proceedings of the National Academy of Sciences*, 2015, **112**, 3269-3274.

37. A. Kozlov, J. Gröbner and R. Schmid-Fetzer, *Journal of Alloys and Compounds*, 2011, **509**, 3326-3337.

38. R. Viennois, C. Colinet, P. Jund and J.-C. Tédenac, *Intermetallics*, 2012, **31**, 145-151.

39. M. Riffel and J. Schilz, 1997.

40. P. Leo, J. Lowengrub and H.-J. Jou, *Acta materialia*, 1998, **46**, 2113-2130.

41. S. Hu and L. Chen, *Acta materialia*, 2001, **49**, 1879-1890.

42. L. Q. Chen and J. Shen, *Computer Physics Communications*, 1998, **108**, 147-158.

43. E. N. Nikitin, E. N. Tkalenko, V. K. Zaitsev, A. I. Zaslavskii and A. K. Kuzentsov, *Inorg. Mater.*, 1968, **4**, 1656-1659.

44.   S. F. Muntyanu, E. B. Sokolov and E. S. Makarov, *Inorg. Mater.*, 1966, **2**, 740-744.

45.   I.-H. Jung, D.-H. Kang, W.-J. Park, N. J. Kim and S. Ahn, *Calphad*, 2007, **31**, 192-200.

46.   N. Saunders and A. P. Miodownik, *CALPHAD (calculation of phase diagrams): a comprehensive guide*, Elsevier, 1998.

47.   J. W. Gibbs, *Scientific Paper, Vol1, Thermodynamics*, Dover, New York, 1961.

48.   L. Tisza, 1961.

49.   J. W. Cahn and F. Larché, *Acta Metallurgica*, 1984, **32**, 1915-1923.

50.   J.-Y. Huh and W. Johnson, *Acta metallurgica et materialia*, 1995, **43**, 1631-1642.

51.   H. Kasai, L. Song, H. L. Andersen, H. Yin and B. B. Iversen, *Acta Crystallographica Section B: Structural Science, Crystal Engineering and Materials*, 2017, **73**, 1158-1163.

52.   D. Zhou, J. Liu, S. Xu and P. Peng, *Computational Materials Science*, 2012, **51**, 409-414.

53.   S. Ganeshan, S. Shang, H. Zhang, Y. Wang, M. Mantina and Z. Liu, *Intermetallics*, 2009, **17**, 313-318.

54.   M. Manuel, A. Singh, M. Alderman and N. Neelameggham, *Magnesium Technology 2015*, Springer, 2016.

TOC
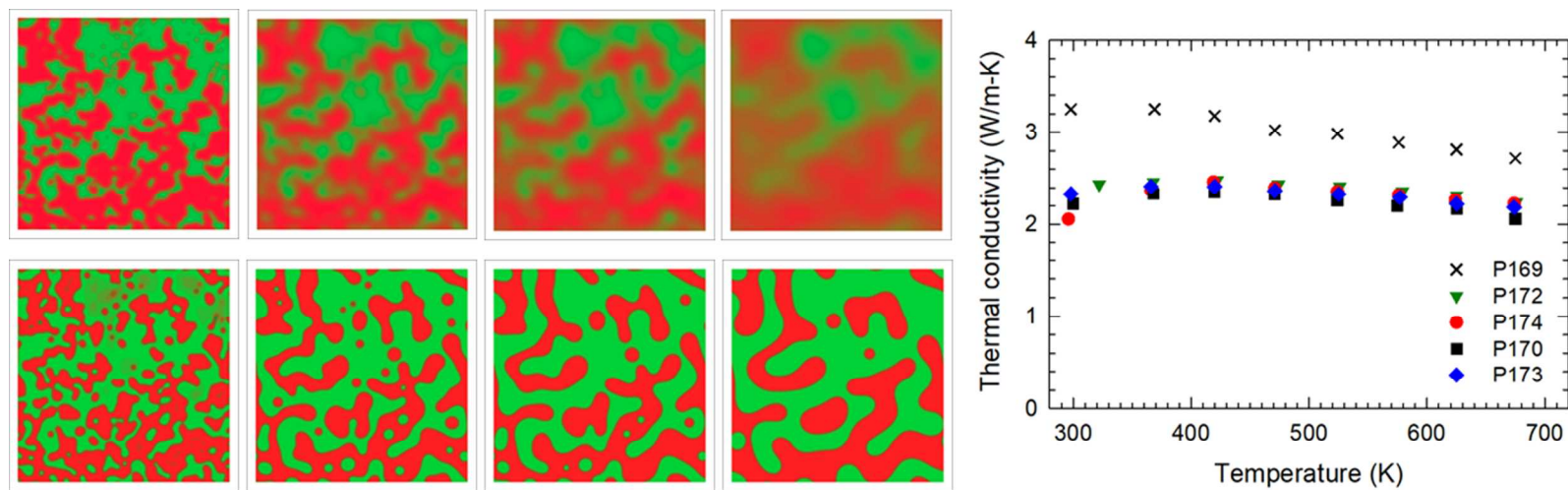
Strain-induced suppression of the miscibility gap in solid solutions of Mg_2Si and Mg_2Sn was studied for suppressing lattice thermal conductivity.